Oral presentation | Industrial applications

Industrial applications-II

Tue. Jul 16, 2024 10:45 AM - 12:45 PM Room B

[4-B-02] On the Aerodynamic Instability in a Multistage Axial-centrifugal Combined Compressor

*Cheng Tian[1], Song Fu[1] (1. Tsinghua University)

Keywords: Combined Compressor, Multistage, Rotating Instability, URANS

Twelfth International Conference on Computational Fluid Dynamics (ICCFD12), Kobe, Japan, July 14-19, 2024

On the Aerodynamic Instability in a Multistage Axial-centrifugal Combined Compressor

Cheng Tian*, Song Fu*
Corresponding author: fs-dem@tsinghua.edu.cn
* Tsinghua University, China.

ABSTRACT

Axial-centrifugal combined compressors are prevalent in small and medium aero-engines. However, the understanding of aerodynamic instability in combined compressors lags behind that in pure axial compressors. This study conducts a numerical investigation of the unstable flow within a multistage combined compressor which consists of three axial stages and one centrifugal stage, utilizing a full annulus simulation. Compared between CFD-predicted and experimental data, the relative error of compressor performance is approximately 2%. Rotating instability is identified in the first axial rotor at 70% of the design speed. A discernible hump in the frequency spectrum is detected by pressure probes positioned near the leading edge of R1. The frequency of rotating instability falls between 4/15 and 12/15 of the blade passing frequency. The axial extent of rotating instability is confined to the inlet guide vane and the first axial rotor. The filtered pressure signal indicates that the disturbances rotate at around 50% of the rotor rotational speed. The rotating instability is induced by the instability of tip vortices near the leading edge of the first rotor.

INTRODUCTION

Axial-centrifugal combined compressors are widely used in small and medium aero-engines, including notable instances such as PWC's PT6, GE's T700, and Chinese AES100 engines. In small and medium engines, centrifugal compressors exhibit high single-stage pressure ratio and efficiency. However, when it comes to multistage, if only centrifugal stages are used, the flow path would be very complex and it would be difficult to maintain high efficiency. Consequently, the number of centrifugal stages usually does not exceed two, which in turn restricts the pressure ratio of the entire compressor. To achieve higher pressure ratio, one approach is to incorporate several axial stages before the centrifugal stage, thereby leading to axial-centrifugal combined compressors.

The requirement for the high pressure ratio in modern compressors is progressively increasing, consequently leading to the possibility of serious aerodynamic instability issues such as rotating instability (RI), rotating stall, and surge. However, compared to axial compressors, there has been relatively limited research conducted on the stability of combined compressors. In the previous investigation from the same authors[1], RI was observed in the first rotor of a combined compressor despite that the entire compressor operates stably. Thus, the current paper focuses on the characteristics of RI.

RI was first noticed by Mathioudakis and Breugelmans[2], who observed "the simultaneous existence of disturbances of different wavelengths.". The typical phenomenon of RI is a pre-stall perturbation with small circumferential extent, rotating at approximately half the rotor speed in the same rotational direction, possessing a high circumferential count, and exhibiting variations in intensity, wave number, and frequency[3]. The frequency spectrum associated with RI exhibits a hump below the blade passing frequency. RI could increase the risk of blade fracture and generate broadband noise.

Mailach et al.[4] did an experimental investigation and observed RI near the stability limit. They believed that RI was caused by periodical interactions of the tip clearance flow of one blade and the flow at the adjacent blade. Vo[5] simulated the flow of RI in a subsonic axial compressor rotor. The backflow of tip clearance fluid from adjacent passages impinged on the pressure surface near the trailing edge and led to RI. Chen et al.[6] applied dynamic mode decomposition to analyze their numerical results of RI in a low-speed axial rotor. RI was composed of pressure waves with various wavelengths and was triggered by the flow interaction of the tip leakage flow. Fujisawa et al.[7] conducted an analysis on the RI in a 1.5-stage axial compressor via both experimental and numerical approaches. They proposed that the RI was generated by the release and separation of the tip leakage vortices. Inoue et al.[8] found the famous 'tornado-like vortex' near the blade tip when small stall cells occurred. This provides a possible view of RI. Im and Zha[9] reported a similar traveling tip vortex structure in a high-speed axial compressor when RI occurred. It was believed to be the source of blade nonsynchronous vibration.

The above researchers all believe that RI is highly related to tip leakage flow. However, Pardowitz et al.[10] proposed RI is caused by shear layer instability resulting from a back-flow in the tip clearance region. Their view was proven by the experimental results of RI in a shrouded axial rotor, where the tip leakage flow was suppressed. Eck et al.[11] further developed this theory. RI was thought to develop from small vortex tubes that behaved like Kelvin–Helmholtz instability when the mass flow rate was small enough.

Despite the significant progress that has been made in prior research, the flow mechanism of the RI remains unclear, especially for axial-centrifugal combined compressors. The current paper aims to study the flow structure and physical mechanism of RI in a multi-stage axial-centrifugal combined compressor through the approach of computational fluid dynamics (CFD).

This paper is structured as follows. Firstly, the examined compressor and the details of numerical settings will be presented. Subsequently, a comparison will be made between the compressor performance parameters obtained through experiments and CFD. Additionally, a detailed analysis of RI will be performed. Lastly, conclusions will be drawn.

METHODOLOGY

This study numerically investigates the flow characteristics in a multistage combined compressor which consists of three axial stages and one centrifugal stage, along with inlet and outlet guide vanes. This compressor was designed and tested by Zhuzhou Liulingba Technology & Science Company in China[12]. To capture the asymmetric unstable flow, a computational domain covering the full annulus space is employed, as illustrated in Figure 1. Structured grids are generated by NUMECA Autogrid5, resulting in approximately 357 million cells. Table 1 lists the detailed distribution of grids in each blade row, along with the blade number. For brevity, the entire compressor is abbreviated as 3A1C, and blade rows are labeled accordingly in Table 1.

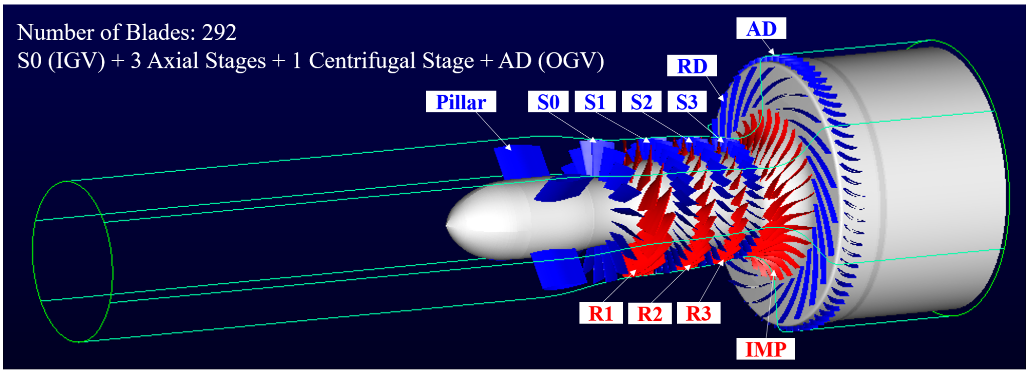

Figure 1: Computational Domain of 3A1C Compressor.

The simulation adopts the URANS algorithm within an in-house CFD solver, which has been previously verified in various compressors[13, 14, 1]. The shear stress transport (SST) $k-\omega$ turbulence model is applied, operating with a second-order accuracy numerical method. Inviscid fluxes are discretized with the MUSCL reconstruction and the rotated Roe scheme[15], while viscous fluxes are evaluated via the second-order central scheme. Time integration is achieved using the implicit lower-upper symmetric Gauss-Seidel (LUSGS) scheme with sub-iterations in pseudo time. 1500 physical time steps are included in each revolution period. In other words, 100 time steps are used for each blade passing period of the first axial rotor (R1). The rotational speed is set at 24150 rounds per minute, equivalent to 70% of the compressor's designed speed. Flow simulations in rotors and stators are conducted in different reference frames: rotating and static, respectively. The sliding mesh method is implemented at rotor-stator interfaces to ensure the high fidelity of unsteady simulations.

Row Name	Abbreviation	Blade Number	Annulus Grid Number (10^6)
Inlet Pillar	-	4	11.1
Inlet Guide Vane	IGV or S0	18	26.7
1st Axial Rotor	R1	15	30.2
1st Axial Stator	S1	32	24.9
2nd Axial Rotor	R2	23	29.2
2nd Axial Stator	S2	26	25.4
3rd Axial Rotor	R3	22	29.9
3rd Axial Stator	S3	34	30.6
Centrifugal Impeller	IMP	15 main + 15 splitter	72.8
Radial Diffuser	RD	23	29.5
Outlet Guide Vane	OGV or AD	69	51.4

Table 1: Abbreviation, Blade Number, and Grid Distribution of Each Row

Regarding boundary conditions, atmospheric total pressure and total temperature are specified at the inlet of the computational domain. And the flow is purely along axial direction at the inlet. No-slip and adiabatic conditions are enforced on solid walls. The throttle function[16] is applied at the outlet as follows:

$$P_{out} = P_{atm} + \frac{\dot{m}_{out}^2}{K_t} \tag{1}$$

where P_{out} is the static pressure at the outlet, $P_{atm} = 101325Pa$ is the atmospheric pressure, and $\dot{m}_{out}$ is the mass flow rate at the outlet. K_t is a given coefficient which controls the throttle area. Convergence of unsteady simulations is deemed obtained when the mass flow rate and pressure ratio remain stable in eight revolutions.

The calculation is deemed to have converged when the mass flow rate and overall pressure ratio are stable, and then the flow in eight revolutions is simulated to sample signals. 892 CPU cores are utilized in this study.

RESULTS AND DISCUSSION

This study conducts simulations at two operating points of the compressor, namely choked and near peak efficiency. The performance of the 3A1C compressor has been measured through experiments by ZhuzhouLiulingba Technology & Science Company[12]. This paper presents a comparative analysis between CFD and experimental results on the performance maps, as shown in Figure 2. The relative error on performance parameters of the entire compressor is below 2.2%. The choked operating point has been analyzed in the previous investigation from the same authors[1], and the current paper focuses on the operating point near peak efficiency. It is notable that the present experimental data slightly deviates from those reported in the prior paper due to recent experimental undertakings.

In axial-centrifugal combined compressors, the centrifugal stage is typically the most important component to increase pressure and ensure flow stability. Figure 3 illustrates the normalized static pressure across different streamwise locations at the operating point near peak efficiency. As expected, the CFD results are in good agreement with the experimental data. Despite that the axial section contains more blade rows, about two-thirds of the static pressure increase originates in the centrifugal stage. Figure 4 presents the performance maps of both axial and centrifugal stages in the 3A1C compressor. Notably, the pressure ratio slope within the axial stages remains nearly zero or even positive, implying an unstable operational state[16]. Conversely, the pressure ratio profile within the centrifugal stage exhibits consistency with that of the overall compressor, suggesting that the surge limit of the entire compressor is decided by the centrifugal stage.

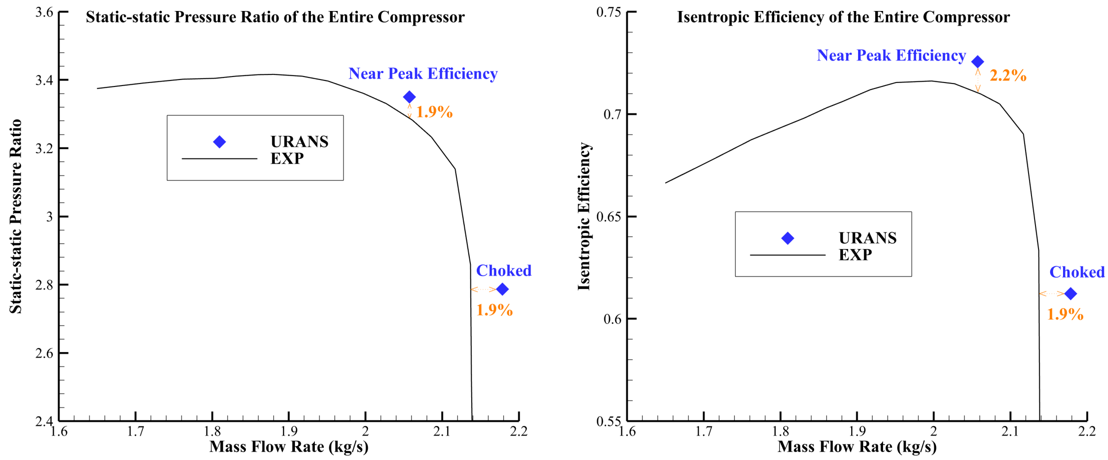

(a) Static-static Pressure Ratio.

(b) Isentropic Efficiency.

Figure 2: Performance Maps of the Entire Compressor.

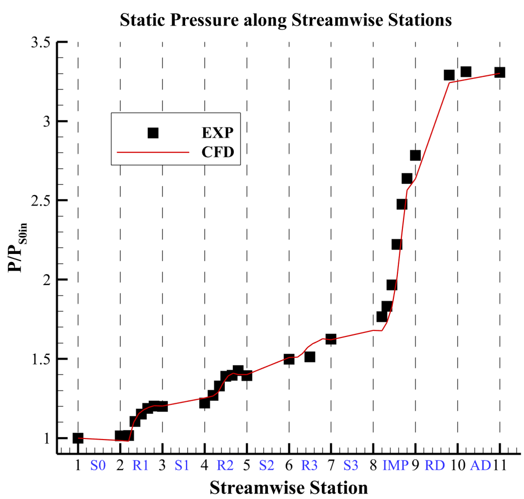

Figure 3: Static Pressure Distribution, Normalized by Pressure at S0 Inlet.

Since the rotational speed is set to 70% of the designed value, the fore stages of the 3A1C compressor are susceptible to encountering flow instability. This phenomenon arises due to inadequate air compression at the low rotational speed, resulting in relatively reduced air density in the rear stages. However, the flow area of the rear stages remains constant, thereby constraining the mass flow rate. Simultaneously, the limited mass flow rate causes small axial velocity, consequently yielding high incidence angles at the fore stages. Ultimately, this sequence of events leads to unstable flow in the fore stages, particularly in R1. Figure 5(a) and Figure 5(b) depict the 3D vortices of the entire compressor and R1 respectively, identified by the Q criterion. It is evident that the tip vortices of R1 propagate upstream of the leading edge of R1 blades, which is a characteristic phenomenon that indicates flow instability in axial compressors. Nonetheless, in this combined compressor, the centrifugal stage serves to sustain overall stability and even preserve near-peak efficiency. The instability observed within R1 can be attributed to a localized flow feature.

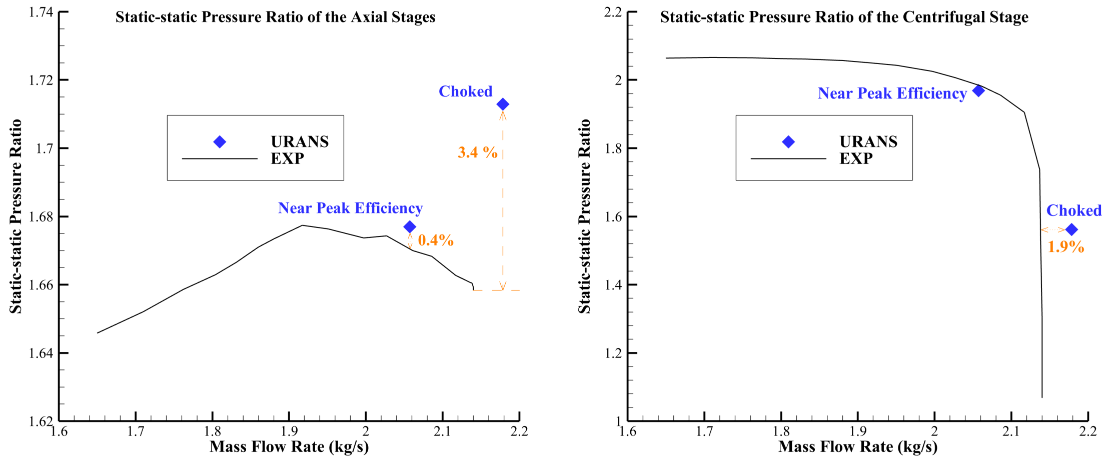

(a) Static-static Pressure Ratio of the Axial Stages. (b) Static-static Pressure Ratio of the Centrifugal Stage.

Figure 4: Performance Maps of Axial and Centrifugal stages.

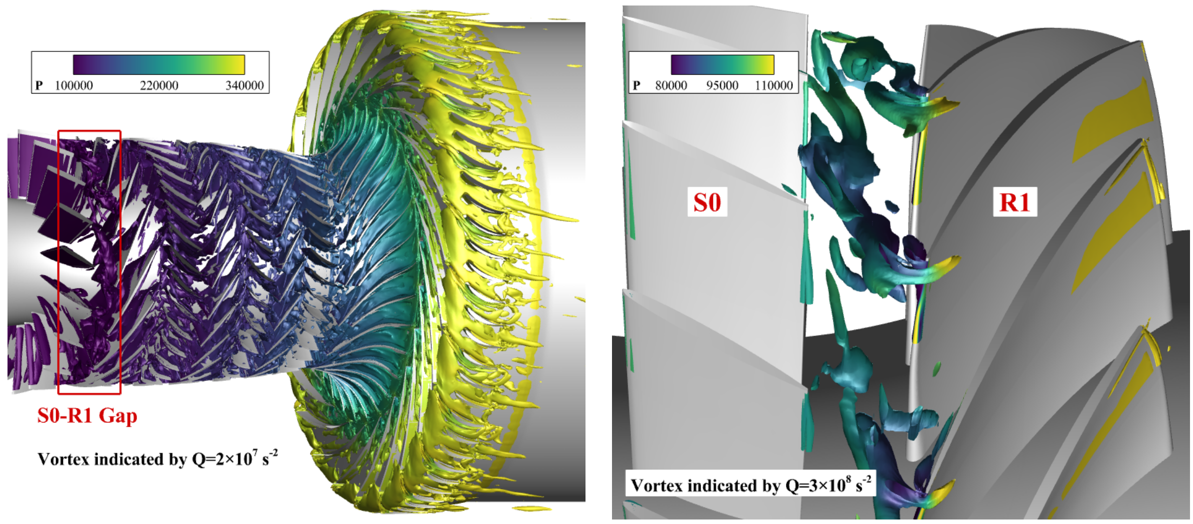

(a) The Entire Compressor. (b) S0-R1 Gap.

Figure 5: 3D Vortices Identified by the Q Criterion, Colored By Pressure.

To detect the flow of R1 tip vortices, several probes capable of capturing transient pressure are installed on the casing adjacent to the blade leading edge of R1 during the experiment. This methodology is also replicated in CFD simulations. Despite the CFD simulation being conducted in the rotating reference frame, the numerical pressure probes are fixed in the static reference frame. The power spectral density (PSD) of the pressure signals obtained from the experiment and CFD is calculated with Welch method, and the outcomes are shown in Figure 6. The two distinct peaks denote the blade passing frequency (BPF) of R1 and its harmonic. The BPF of R1 is 15 times the rotor rotating frequency (RRF) due to the presence of 15 blades in R1. Beneath the BPF, a discernible hump emerges in the frequency ranging between 4 and 12 times the RRF. This feature is indicative of RI[3].

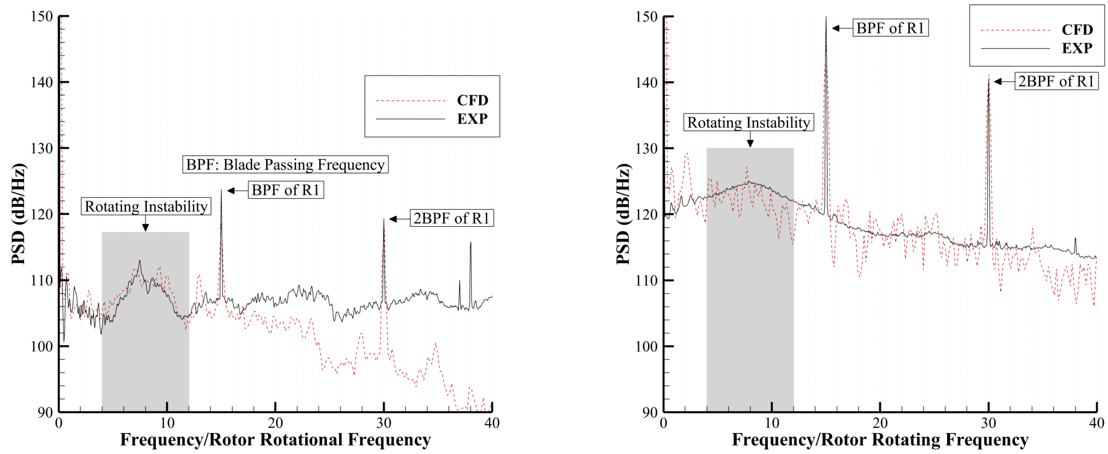

(a) S0 Inlet.

(b) R1 Leading Edge.

Figure 6: Power Spectral Density of Pressure on Casing.

In CFD simulations, a large number of pressure probes are positioned on the casing adjacent to the R1 blades to investigate the RI in detail. The axial placements of these probes are shown in Figure 7. In the circumferential direction, probes are spaced at intervals of two degrees. It is noteworthy that the depiction of the R1 blades in Figure 7 is merely schematic, as no physical rotor blade exists on the casing. All numerical probes are fixed in the static reference frame. Through such a dense array, the propagation of disturbances caused by RI can be effectively tracked and analyzed.

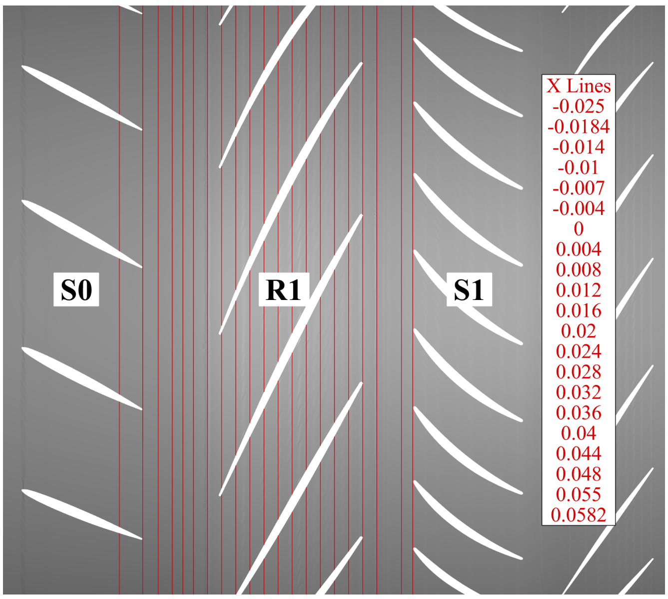

Figure 7: Axial Positions of Numerical Probes on Casing near R1.

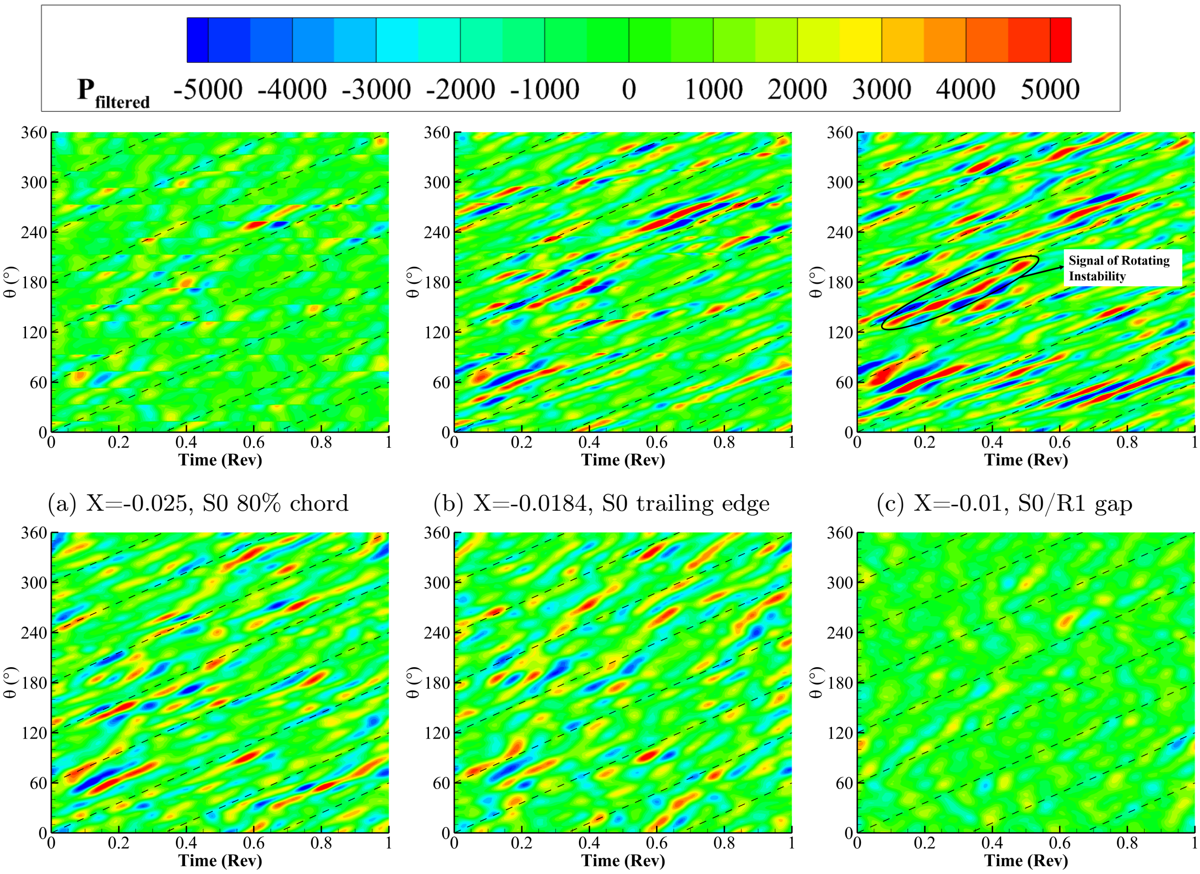

(a) X=-0.025, S0 80% chord
(b) X=-0.0184, S0 trailing edge
(c) X=-0.01, S0/R1 gap
(d) X=-0.004, S0/R1 gap
(e) X=+0.004, R1 leading edge
(f) X=+0.02, R1 45% chord

Figure 8: Propagation of RI, Indicated by Contour of Pressure Filtered between 4 and 12 RRF. Dashed Black Lines Represent 50% Rotational Speed of Rotor.

The pressure obtained from numerical probes is filtered between 4 and 12 RRF, and the results are illustrated in Figure 8. The horizontal axis of this figure denotes time, while the vertical axis represents the circumferential coordinate. In Figure 8(a), some discontinuities are observable along the circumferential direction, attributed to the obstruction caused by the S0 blades. Figures 8(b)(c) and (d) exhibit apparent signals aligning with the dashed black lines, which indicate flow structures propagating along the annulus at 50% of the rotor's rotational speed. An example is circled in Figure 8(c). These signals are believed to be indicative of RI. The circumferential extent of each signal, and the count of signals in the annulus both display variability, reflecting the inherent unsteadiness of RI. In Figure 8(a), they are truncated by the S0 blades. In Figure 8(e), they are significantly affected by the R1 blades, and the propagating speed falls between 50% and 100% of the rotor's rotational speed. In Figure 8(f), nearly all signals vanish. Consequently, it can be inferred that RI primarily occurs in the axial gap between S0 and R1.

Figure 9 depicts vectors of velocity in the rotating reference frame at various blade heights, accompanied by contours of the static pressure. Solid vectors denote velocities with a positive radial component, while translucent vectors denote velocities with a negative radial component. At 50% and 70% blade height (Figure 9 (a) and (b)), the airflow adheres closely to R1 blade profiles without experiencing any discernible flow separation. At 80% blade height (Figure 9 (c)), the flow is generally smooth, but the local fluid near the leading edge of R1 blades is influenced by tip vortices. Beyond 90% blade height (Figure 9 (d)-(f)), the leading-edge spillage flow of R1 blades becomes evident, without the occurrence of backflow near the trailing edge. It can be inferred that the tip clearance flow of R1 plays an important role in the RI phenomenon of this compressor.

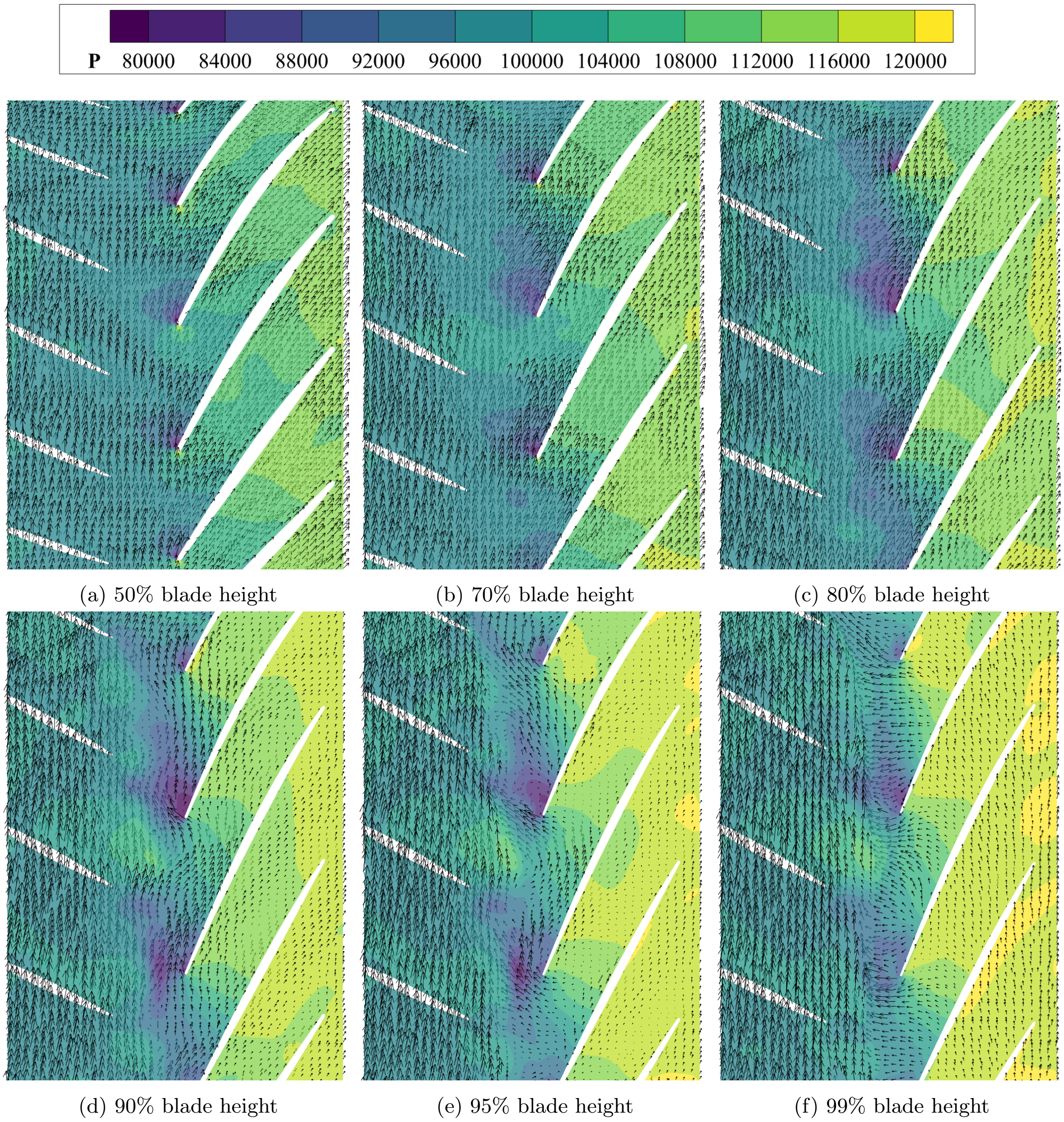

Figure 9: Velocity Vectors in the Rotor and Contours of Static Pressure at Different Blade Heights, Viewed in the Rotating Reference Frame.

The tip clearance flow of R1 is illustrated in Figure 10, with the inclusion of only three R1 blades for clarity. In Figure 10(b), the black and red lines represent streamlines that pass through the fore and rear parts of blade A's tip clearance, respectively. The fore and rear parts of blade A are distinguished by the vertical projection of blade B's leading edge onto blade A's suction surface. In the fore part of blade A's tip clearance, the air flows almost perpendicular to the blade surface, subsequently rolling into the tip vortices. The tip vortices are pushed upstream of the leading edge plane by tip leakage flow, resulting in leading-edge spillage. The tip vortices extend upstream of the leading edge plane rather than downstream, thereby losing their stability. It is believed that RI arises from the instability of these tip vortices. In the rear part of blade A's tip clearance, the air flows towards blade B's tip clearance, causing secondary leakage.

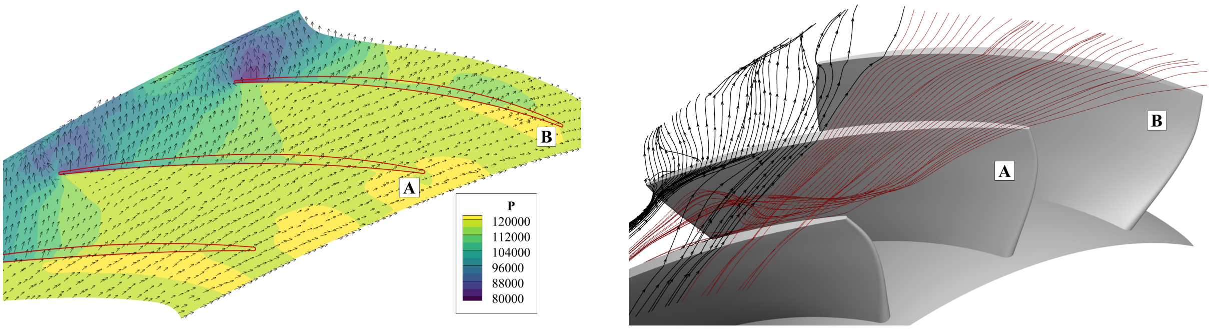

(a) Velocity Vectors and Contour of Static Pressure.

(b) 3D Streamlines.

Figure 10: Flow in the Blade Tip Clearance of R1, Viewed in the Rotating Reference Frame.

CONCLUSIONS

In this paper, a full annulus URANS simulation is conducted on a combined compressor containing three axial stages and one centrifugal stage. The compressor performance parameters show good agreement between CFD and experimental results. The current study is primarily centered on the rotating stability (RI) phenomenon. The main findings are summarized as follows:

1. RI phenomenon occurs even under conditions where the entire compressor operates near peak efficiency at the 70% rotational speed line. A discernible hump in the frequency spectrum is detected near the leading edge of R1, with the frequency between 4/15 and 12/15 of BPF.

2. RI structures mainly reside in the gap between S0 and R1, spanning over 80% blade Height, and propagate along the annulus at a rate of approximately 50% of the rotor's rotational speed.

3. The tip leakage flow of R1 induces the upstream displacement of tip vortices beyond the leading edge plane, consequently causing leading-edge spillage. RI is generated due to the instability of these tip vortices.

Constrained by the accuracy of URANS, the details of tip vortices remain insufficient. In the future, the authors will focus on the phenomenon of rotational instability in this compressor through methods with higher resolution.

References

[1] Cheng Tian and Song Fu. Full annulus simulation on a multistage axial-centrifugal combined compressor. *Proceedings of GPPS International Technical Conference*, 2023.

[2] K. Mathioudakis and F. A. E. Breugelmans. Development of small rotating stall in a single stage axial compressor. *Proceedings of ASME International Gas Turbine Conference and Exhibit*, 1985.

[3] I. J. Day. Stall, surge, and 75 years of research. *Journal of Turbomachinery*, 138(1), 2016.

[4] R. Mailach, I. Lehmann, and K. Vogeler. Rotating instabilities in an axial compressor originating from the fluctuating blade tip vortex. *Journal of Turbomachinery*, 123(3):453–460, 2001.

[5] Huu Duc Vo. Role of tip clearance flow in rotating instabilities and nonsynchronous vibrations. *Journal of Propulsion and Power*, 26(3):556–561, 2010.

[6] Xiangyi Chen, Björn Koppe, Martin Lange, Wuli Chu, and Ronald Mailach. Influence of casing groove on rotating instabilities in a low-speed axial compressor. *Journal of Turbomachinery*, 145(7):071015, 2023.

[7] Nobumichi Fujisawa, Yutaka Ohta, Mai Yamagami, Takashi Goto, and Dai Kato. Unsteady flow mechanism of a rotating instability in a 1.5-stage axial compressor. *Proceedings of GPPS International Technical Conference*, 2023.

[8] M. Inoue, M. Kuroumaru, T. Tanino, S. Yoshida, and M. Furukawa. Comparative studies on short and long length-scale stall cell propagating in an axial compressor rotor. *Journal of Turbomachinery*, 123(1):24–30, 2001.

[9] Hongsik Im and Gecheng Zha. Investigation of flow instability mechanism causing compressor rotor-blade nonsynchronous vibration. *AIAA Journal*, 52(9):2019–2031, 2014.

[10] Benjamin Pardowitz, Antoine Moreau, Ulf Tapken, and Lars Enghardt. Experimental identification of rotating instability of an axial fan with shrouded rotor. *Proceedings of the Institution of Mechanical Engineers, Part A: Journal of Power and Energy*, 229(5):520–528, 2015.

[11] Mario Eck, Silvio Geist, and Dieter Peitsch. Physics of prestall propagating disturbances in axial compressors and their potential as a stall warning indicator. *Applied Sciences*, 7(3):285, 2017.

[12] Gaiqi Li, Dongyang Ma, Du Li, Shaorong Liu, and Yanmei Yang. Surge test on newly developing civil turboshaft engine under take-off condition (in Chinese). *Acta Aeronautica et Astronautica Sinica*, 44(14):628190, 2023.

[13] Ke Shi and Song Fu. Study of shock/blade tip leakage vortex/boundary layer interaction in a transonic rotor with IDDES method. *Proceedings of ASME Turbo Expo*, 2013.

[14] Siya Jiang, Cheng Tian, and Song Fu. Evolution of unsteady vortex structures and rotating stall cells in a centrifugal compressor with vaneless diffuser. *Proceedings of GPPS International Technical Conference*, 2021.

[15] Yuxin Ren. A robust shock-capturing scheme based on rotated Riemann solvers. *Computers & Fluids*, 32(10):1379–1403, 2003.

[16] N. A. Cumpsty. Compressor aerodynamics. *Longman Scientific & Technical*, 1989.